Desalination 523 (2022) 115449

Contents lists available at ScienceDirect

Desalination

journal homepage: www.elsevier.com/locate/desal

Recyclable and efficient ocean biomass-derived hydrogel photothermal evaporator for thermally-localized solar desalination

Yanpei Tian [a], Xiaojie Liu [a], Shilin Xu [a], Jiansheng Li [a], Andrew Caratenuto [a], Ying Mu [a], Ziqi Wang [a], Fangqi Chen [a], Ruizhe Yang [b,c], Jun Liu [b,c], Marilyn L. Minus [a], Yi Zheng [a,*]

[a] Department of Mechanical and Industrial Engineering, Northeastern University, Boston, MA 02115, USA
[b] Department of Mechanical and Aerospace Engineering, University at Buffalo, The State University of New York, Buffalo, NY 14260, USA
[c] RENEW (Research and Education in Energy, Environment, and Water) Institute, University at Buffalo, NY 14260, USA

HIGHLIGHTS

- An agar-based hydrogel photothermal evaporator for interfacial solar desalination.
- Achieve an evaporation rate of 5.15 kg m^{-2} h^{-1} in 3.5 wt% NaCl solution under 1 sun.
- Vertically arranged channels assist water pumping and salt rejection.
- The hydrogel evaporator can be easily recycled to extend its lifespan.

GRAPHICAL ABSTRACT

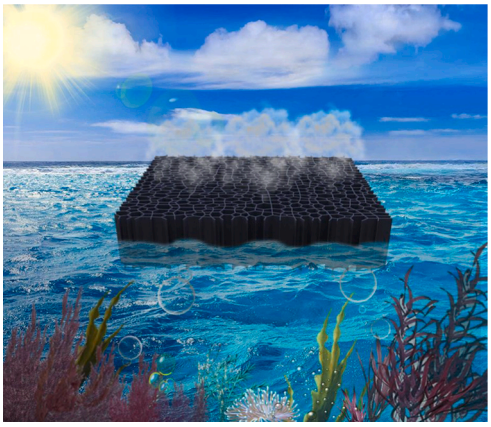

ARTICLE INFO

Keywords:
Ocean biomass
Solar desalination
Agar
Plant transpiration
Recyclability
Vertically aligned microchannels

ABSTRACT

Interfacial evaporation is gaining popularity as a facile and effective method for harvesting solar energy and yielding freshwater from sewage and seawater. However, challenges exist for achieving a balance among a plethora of performance metrics, e.g., low cost, high evaporation efficiency, off-grid deployment, and negligible environmental impact. In this study, a hydrogel evaporator is prepared by combining agar, naturally abundant ocean biomass, with titanium nitride nanoparticles. Due to the excellent photothermal conversion effect of titanium nitride nanoparticles, the evaporator shows a solar absorptance of 0.98. This evaporator has vertically aligned water channels and is fabricated by an ice template-induced self-assembly method, enabling the formation of a biomimetic wood structure. The rapid water transport and salt drainage within its aligned channels, effective water activation in hydrogel molecular meshes, and efficient heat localization allow this hydrogel evaporator to achieve an evaporation rate of 5.15 kg m^{-2} h^{-1} under the irradiance of one sun (1 kW m^{-2}). The indirect water supply method using cotton wipe as the water transportation channels and polystyrene foam as the thermal barrier efficiently localize heat within the top small evaporation region, which ensures such a high

* Corresponding author.
E-mail address: y.zheng@northeastern.edu (Y. Zheng).

https://doi.org/10.1016/j.desal.2021.115449
Received 13 August 2021; Received in revised form 7 November 2021; Accepted 10 November 2021
Available online 17 November 2021

evaporation rate. Moreover, this hydrogel evaporator is easy to be recycled without performance reduction to achieve an extended lifespan with the advantage of facile thermal recyclability after long-term utilization. The freeze-thawing fabrication of this hydrogel evaporator is feasible for scalable deployment. This work offers new possibilities for high-quality freshwater yields with cost-effective raw materials and deployable solar desalination systems for industrial implementations.

1. Introduction

The ever-increasing freshwater scarcity, brought about by rapid industrial development and fast-growing populations, is one of the most prevalent issues affecting people [1]. Currently, about four billion people have limited access to freshwater [2]. Water purification techniques from seawater or wastewater are emerging as promising solutions to alleviate this freshwater shortage due to its cost-effectiveness, low energy consumption, and minimal environmental footprint [3]. Reverse osmosis and thermal vapor distillation, the most widely employed desalination technologies, are unfeasible in off-grid regions and underdeveloped countries because their high electricity consumption and complex infrastructure make them energy- and capital-intensive [4]. Solar desalination, utilizing abundantly available solar energy to facilitate seawater evaporation, has gained growing attention due to its sustainability and environmentally benignity [5]. An economically feasible solar-driven water desalination system should possess a high rate of freshwater yield with assured water quality while also being affordable to communities in water-scarce areas that cannot afford expensive infrastructure installations [6–8]. Traditional solar desalination suffers from a low evaporation rate and evaporation efficiency by dispersing photothermal materials directly into the water for bulk heating [9]. Recently, interfacial solar desalination has achieved enhanced evaporation rates and energy efficiency by confining the heat to the air-water interface for minimizing the heat loss associated with bulk heating [10–12]. The design principles for an efficient solar evaporator have been recognized: 1) developing effective solar absorbing materials for enhanced photothermal effects, 2) optimizing heat localization to confine the heat within the evaporation region, 3) designing unhindered water channels for both quick water transportation and fast salt rejection, 4) accelerating vapor release [13,14]. Various materials with different configurations have been developed for interfacial solar desalination, such as 1D nanofibers [15–17], 2D membranes [18,19], 3D photothermal aerogels [20,21], and hierarchical porous hydrogels [22,23]. For instance, cow dung cakes [24,25], blue metal stones [26], marble pieces [27], and hybrid graphene/TiO_2 nanoparticles [28,29] are investigated as thermal energy storage to enhance the distillate output. Among these, the hydrogel-based evaporator is most promising. It has been demonstrated to yield a high evaporation rate of 4.0 kg m^{-2} h^{-1} (1 kW m^{-2}) through adjusting the water activation in polymeric networks (polyvinyl alcohol) and tailoring the wettability states of solar evaporation surface. However, hydrogel evaporators still face problems of cost-effectiveness, recyclability, and resource sustainability [30]. The fabrication processes of polyethylene glycol, polyvinyl alcohol, and poly (sodium acrylate) derived hydrogel evaporators are complicated, and these materials cannot be recycled. This would limit their application for long-term durability, thus increasing the cost and environmental concern. For large-scale engineering applications, the fabrication process should be straightforward with less energy or materials consumption to make the products competitive. Moreover, the recyclability of the composites is an issue after the ending of the lifespan. If the composites can be recycled with simple processes to extend their lifespan, the overall cost of the photothermal evaporator will be reduced to an affordable degree for less-developed regions. Therefore, considering both ecosystem sustainability and cost-effectiveness, a biomass-derived hydrogel that can be extracted from abundant raw ocean biomass and recycled using simple thermal-melting and re-casting techniques provides a perfect alternative for sustainable and scalable solar desalination systems [31,32].

Agar consists of the natural linear polysaccharide agarose and a heterogeneous mixture of agaropectin that can be extracted commercially from seaweed such as Gelidiaceae and Gracilaria, both of which are abundant in the ocean (Fig. 1a) [33]. The ocean biomass is eco-friendly, cost-effective, non-toxic, and biodegradable, which has been commonly employed as a thickener, emulsifier, stabilizer, and gel-forming agent in the industrial fabrication processes [34]. Furthermore, agar can be easily thermally recycled after long-term utilization without sacrificing the performance [35]. Plant transpiration is a natural process involving water movement from underground to the atmosphere and water evaporation from aerial plant features, such as leaves and stems [36]. Water is passively transported first into the roots, followed by the xylem. Meanwhile, the negative pressure coming from the potential difference of the water and capillary force pumps water up to the leaves through the vertically aligned vessels and tracheids in the tree trunk. Moreover, under solar irradiance and air convection, transpiration is enhanced by heating the water in the leaves, enhancing the vaporization of water into the atmosphere through stomas in the leaf epidermis. Therefore, plant transpiration consists of water transportation through the trunk and water evaporation through the leaves, which shares similar processes of solar desalination. The vertical channels within the tree trunk are the result of natural selection after millions of years, and this offers us an approach to artificially imitating its natural aligned structures to increase the water transportation rate instead of employing the randomly distributed channels in hydrogel [22,23,30].

Herein, mimicking the water transportation process within a tree trunk, we demonstrate an effective ocean biomass-derived hydrogel solar evaporator for continuous and long-term desalination with vertically aligned water channels for rapid water transportation and tunable water content for regulating water absorption. Fabrication is achieved by ice-template self-assembly and freeze-drying assisted formation of vertical microchannels in the agar hydrogel, and titanium nitride (TiN) nanoparticles serve as a solar-harvesting material transferring solar energy to heat. The rapid water transportation of the agar and TiN hydrogel-based evaporators (ATHEs) arises from the hydrophilic functional groups of polymeric chains as well as the capillary forces within the biomimetic wood structures. The hydrogel also enhances the water activation in polymeric molecular meshes to significantly reduce the enthalpy of water evaporation. The porous structures with low thermal conductivity facilitate the localization of heat within the evaporation surface, thereby suppressing the heat loss dissipation down to the bulk water. With these advantageous features of efficient photothermal conversion, sufficient water transport, effective water activation, strong heat localization, and quick salt drainage, the ATHEs have been demonstrated to yield an evaporation rate of 5.15 kg m^{-2} h^{-1} under one sun illumination. Besides, ATHEs exhibit excellent long-term stability for continuous freshwater production and superior recyclability to extend their lifespan and enhance their cost-effectiveness. This nature-inspired and ocean biomass-derived solar evaporator facilities a sustainable approach for highly efficient desalination that can allow a variety of communities to own access to high-quality freshwater.

2. Experimental section

2.1. Materials

Agar was purchased from Innovating Science. TiN nanoparticles

(99.2%, 80 nm in diameter, cubic) were supplied by US Research Nanomaterials, Inc. NaCl (99.0%) was provided by Sigma-Aldrich. Cotton wipes used as the water pathways were supplied by Webril. The polystyrene (PS) insulation foam with a thickness of 25 mm was purchased from the McMaster-Carr and the polyethylene (PE) foam with a thickness of 5 mm was supplied by Foam Factory inc.

2.2. Sample preparations

The ATHE 2 sample was prepared as follows: 1 g agar powder and 0.5 g TiN nanoparticles were dissolved in 100 g deionized water at 90 °C under mechanical stirring 1 h to form the homogeneous hydrogel solution. The obtained hydrogel solution was poured into a glass petri dish and cooled down to room temperature to form the agar/TiN hydrogel with a thickness of about 8 mm. Then, the agar/TiN hydrogel was placed on top of a cold copper cylinder which was pre-cooled by the surrounding liquid nitrogen (N_2). During the cooling process, the agar/TiN hydrogel was unidirectionally frozen and the ice crystals grew along the temperature gradient which is perpendicular to the surface of the copper cylinder. This formed vertically microchannels within the agar/TiN hydrogel. After freeze-drying for 48 h in the freeze drier (Labconco-195) at a temperature of −85 °C, the cryogel was obtained. The ATHE 1 and ATHE 3 samples were fabricated following the same procedures, but instead adding 0.5 g agar/0.25 g TiN nanoparticles and 2 g agar/0.5 g TiN nanoparticles, respectively, to form different hydrogel solutions. The ATHE 2 sample prepared by the freeze-thaw method was fabricated by freezing the agar/ TiN hydrogel solution with liquid N_2 and thawed in deionized water at 20 °C for 1 h. We repeated this freeze-thaw process ten times to obtain the cryogel. The obtained ATHEs are soaked into a 2 wt% calcium chloride solution for 12 h to enhance the water supply speed. The ATHE devices were fabricated as follows: A 10 mm thick PS foam was cut into a circle of 4.5 cm in diameter. The cotton wipe (5 cm × 3 cm) was soaked in the water through a slit of the PS foam, then ATHEs were placed on a cotton wipe with their sides surrounded by PE foam to prevent the water evaporation from sidewalls. The PS foam acts as a thermal barrier between ATHEs and the bulk water, while the PE foam reduces the heat dissipation from the sidewalls of ATHEs. The recycled ATHEs are fabricated by immersing the used ATHEs in deionized water for 24 h to dissolve the salt residuals and redissolve in 90 °C deionized water followed by these processes of the original ATHEs fabrication procedure.

2.3. Experiments of solar evaporation and desalination

Solar evaporation and desalination experiments were performed in the laboratory (temperature: ~21 °C, relative humidity: ~40%) using a solar simulator (Newport, 94081a, 1 kW m^{-2}). The distance between the ATHEs top surface and the optical lens of the solar simulator was

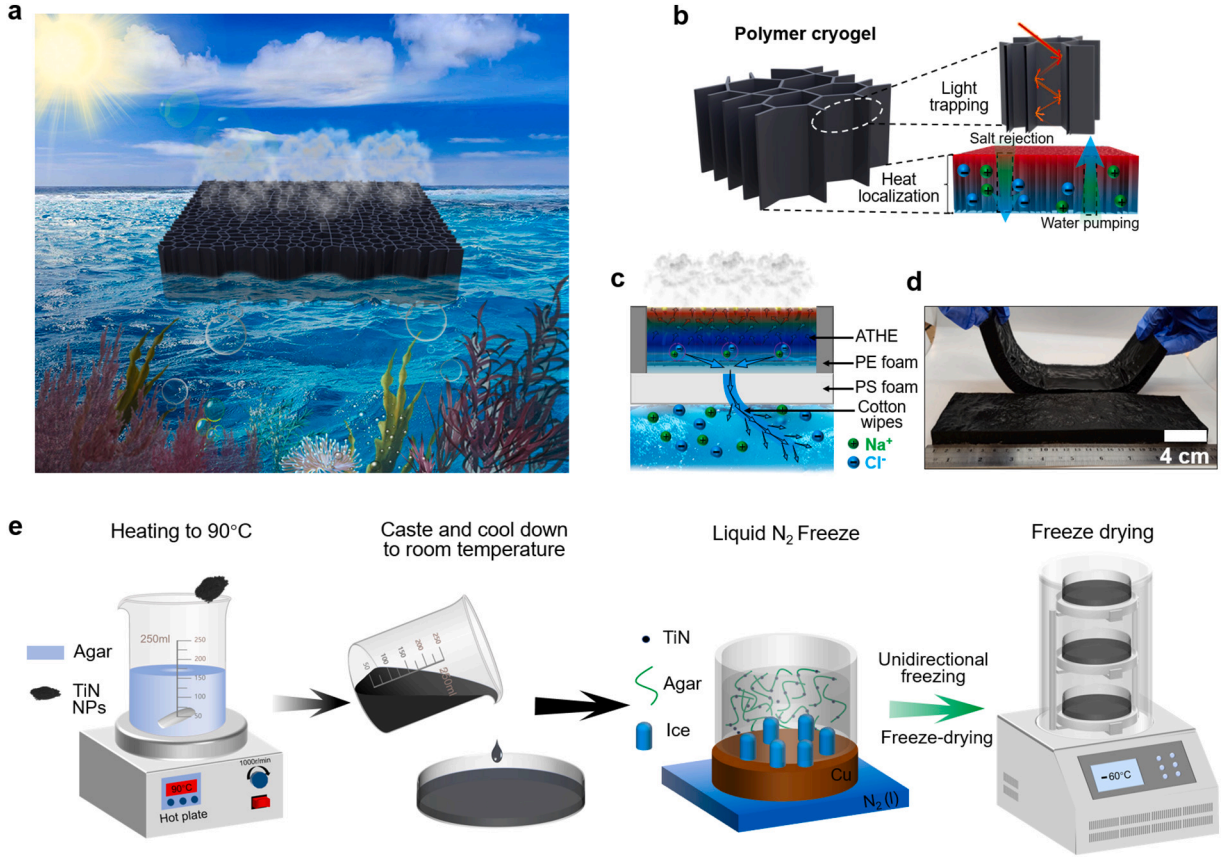

Fig. 1. Schematic illustrations of solar desalination and the fabrication of ATHEs. (a) Schematic elucidating ATHEs involved in solar desalination. ATHEs absorb solar irradiance and float on the sea to produce freshwater. The evaporation occurs on the ATHEs top surface, and the water potential difference pumps water to the top interfacial evaporation regions. The main raw material of ATHEs is agar, extracted from seaweed, such as agarophyte and gracilaria, with vertically aligned water supply channels. (b) The polymer cryogel with vertically aligned light trapping channels efficiently absorbs solar flux. These channels simultaneously serve as water pumping and salt dissipation pathways. The porous structures with low thermal conductivity localize heat in the small region of the water/air interface. (c) Schematic showing the experimental setup. PS foam floating on the water serves as a thermal barrier to reduce the heat dissipation from ATHEs to the bulk saltwater reservoir. The cotton wipe is employed to supply water to ATHEs and dissipate salt to the bulk saltwater. ATHEs are surrounded by PE foam to prevent vapor diffusion from the sidewalls and localize heat within ATHEs. (d) The photograph of a large-scale agar/carbon hydrogel evaporator sheet and its flexibility for application on curved surfaces. (e) ATHEs are synthesized by ice template-induced self-assembly and freeze-drying processes.

adjusted to be 15 cm to keep the input solar flux on the ATHEs surface stable at 1 kW m^{-2}. Before each experiment, the solar flux was calibrated by the TES 132 solar power meter to establish continuity between each experiment. The mass of water was accurately monitored by an electrical scale (RADWAG, PS 1000). The solar desalination experiment with salt water used the same setting while replacing the DI water with the NaCl solution with different salinities. All water evaporation rates were recorded after the solar flux stabilized at one sun for 30 min. For the long-time stability tests of ATHE 2, the water was replaced for each cycle to make sure the initial salinity of saltwater is 3.5%.

2.4. Material characterizations

The reflectance spectra (0.3–2.5 μm) were characterized by a Jasco V770 spectrophotometer with a $BaSO_4$ integrating sphere. The FTIR transmittance spectra were carried on a Jasco FTIR 6600 spectrometer with a diffused gold integrating sphere. The surface morphologies were characterized using a Supra 25 SEM after being coated with a 10 nm gold/palladium mixture layer. The DSC thermograms were measured at a heating rate of 5 °C via the TA DSC Q200. IR thermal images were taken by employing the FLIR A655C thermal camera. Thermal conductivity was characterized with the HotDisk TPS 2500s. The contact angle was measured by a contact angle meter (SINDIN SDC-350). The XRD spectra were characterized from 15° to 100° with a stepsize of 0.02° (Bruker D8 X-ray Diffractometer). High-speed images were imaged by the Chronos 2.1-HD. The optical profilometry images were collected using a Bruker ContourGT-X8 optical profilometer. The solar intensity of the solar simulator was calibrated by the TES 132 solar power meter for each experiment under 0.5, 0.8, 1, and 1.2 kW m^{-2}. The salinity of collected water samples was characterized by the Extech EC400 ExStik salinity meter.

3. Results and discussion

3.1. Fabrications and characterizations of ATHEs

Agar boasts superb water-absorbance, enhanced with the capillary force owing to the vertically biomimetic microchannels. Meanwhile, TiN nanoparticles are excellent photothermal materials with excellent physical and chemical stability. These vertical microchannels serve as perfect light traps to absorb the incident sunlight since the sunlight undergoes multiple reflections and is finally absorbed by the inner walls of ATHEs (Fig. 1b). These channels also act as pathways for water transportation and salt rejection, as well as pumping water to the top evaporation surface and dissipating salt to the bulk water (Fig. 1b). The quick evaporation on the top surface provides water pumping force to facilitate a continuous process of water pumping. The macroporous structure hampers the thermal conductivity of ATHEs, thereby localizing heat to the top region for quick evaporation. Moreover, the vertically aligned microchannels allow vapor to escape without interference. To further improve the evaporation rate of ATHEs, it is placed on top of thermal insulation foam (PS foam) and connected with the cotton wipe, which serves as the water pathway. This design successfully prevents heat from diffusing down to the bulk water (Fig. 1c). The cotton wipe is an excellent water-absorbent, which can synchronously supply sufficient water to ATHEs and dissipate salt ions to the bulk water (Fig. S1†). PE foam is cut to fit the shape of ATHEs and used to prevent both heat and vapor diffusion from the sidewalls of ATHEs. Furthermore, for the large-scale applications, two ATHE samples (25 cm × 8 cm × 1.5 cm) are fabricated and are demonstrated with excellent mechanical flexibility, expanding its potential applications, such as on curved surfaces (Fig. 1d).

The preparation process of ATHEs is shown schematically in Fig. 1e (details are listed in the sample preparation section). First, the agar/TiN hydrogel is prepared by dissolving agar and TiN nanoparticles in 90 °C deionized water and then poured into a glass mold for gelation after following by cooling it down to room temperature. Assisted by a unidirectional ice template process on a cold copper platform cooled by liquid N_2, the vertically aligned microchannels are generated along with the anisotropic ice crystal growth direction (from bottom to up) due to the large temperature difference. After freeze-drying, ATHEs are obtained in a dry state with a gray color (Fig. 2a).

ATHEs can be easily fabricated at a large scale by varying the shape and size of different molds during the gelation. After fully swollen in deionized water, ATHEs with continuous vertically aligned channels shirk and become ultrablack, enabling a high solar absorptance (Fig. 2a). The black color of ATHEs is attributed to TiN nanoparticles which are distributed inside the agar hydrogel network. The TiN nanoparticles show black color with good light absorption across a broad spectrum of wavelengths [37]. Additionally, ATHEs show good mechanical flexibility in their fully-swollen state and they are squeezable and bendable into different shapes, therefore, this flexibility paves the way for real-life engineering applications. Here, ATHEs with different ratios of agar/TiN (0.5 g/0.25 g, 1.0 g/0.5 g, and 2.0 g/0.5 g) in 100 g deionized water are denoted as ATHE 1, ATHE 2, and ATHE 3, respectively.

The top view images of the Scanning electron microscopy (SEM) show a corrugated surface with open pores (Fig. 2b). The top surface with micropores (~100 μm in diameter) facilities the vapor escaping and these micropores services as light traps enhancing the photothermal effects of TiN nanoparticles. TiN nanoparticles absorb sunlight and convert it into thermal energy. Due to the good contact between TiN nanoparticles and agar walls, the absorbed heat can be efficiently transferred to the agar walls and surrounding water for quick evaporation. Agar walls with thicknesses of around 2 μm can be seen in Fig. 2b-1. ATHE 2 possesses vertical tubular interconnected channels with ~50 μm width (Fig. 2c1-2). These vertical microchannels facilitate the pumping of sufficient water from the bulk reservoir to the evaporation surface. Moreover, these channels also function as salt rejection pathways, efficiently dissipating salt to the bulk reservoir. These vertical agar walls have small bumps due to the embedded TiN nanoparticles and large bumps represent some TiN accumulations. Both the well-dispersed TiN nanoparticles and accumulated TiN particles can serve as excellent sunlight traps to boost the photothermal effect (Fig. 2c3-5). The microstructures of ATHE 1 and ATHE 3 are also investigated (Fig. S2†), both of which display vertically aligned channels. The width of those channels can be tuned according to the different concentrations of agar hydrogel solutions. A magnified SEM image demonstrates the surface topographies of TiN nanoparticles and their accumulated particles (Fig. 2c).

Fourier transform infrared (FTIR) spectra elucidate the chemical compositions of ATHEs (Fig. 2f). Peaks at 3417 cm^{-1}, 2902 cm^{-1}, and 1647 cm^{-1} are due to the stretching vibrations of $-NH_2$ and $-OH$ groups, the asymmetric stretching of $-CH_3$, and the bending vibration from the $-NH_2$ group and the stretching vibration from the $-C{=}O$ group [38]. These abundant $-OH$ and $-NH_2$ groups indicate hydrophilic features of the pure agar hydrogel and ATHEs. The 1375 cm^{-1} band is ascribed to the $-CH_3$ symmetrical deformation mode. Peaks at 1163 cm^{-1} and 1072 cm^{-1} result from the $C{-}O$ stretching vibrations ($C{-}O{-}C$) of aliphatic ether [39]. TiN does not show an obvious absorption band in the FTIR spectra. According to the X-ray diffraction (XRD) spectra, the diffraction peak at the 2θ value of 19° substantiates the presence of agar in ATHE 2 [40], and the diffraction peaks at 2θ values of 36.7°, 42.5°, 61.9°, 74.2°, and 78.1° are indexed as the cubic cell of TiN nanoparticles (Fig. 2g) [41].

3.2. Tunable water transportation, solar absorption, and heat localization of ATHEs

One of the significant points to achieve a high solar-driven evaporation rate is to efficiently absorb the solar irradiance. Owing to the TiN nanoparticles existing in the agar hydrogel networks and the effective light trapping effects within the microchannels of ATHEs, it exhibits

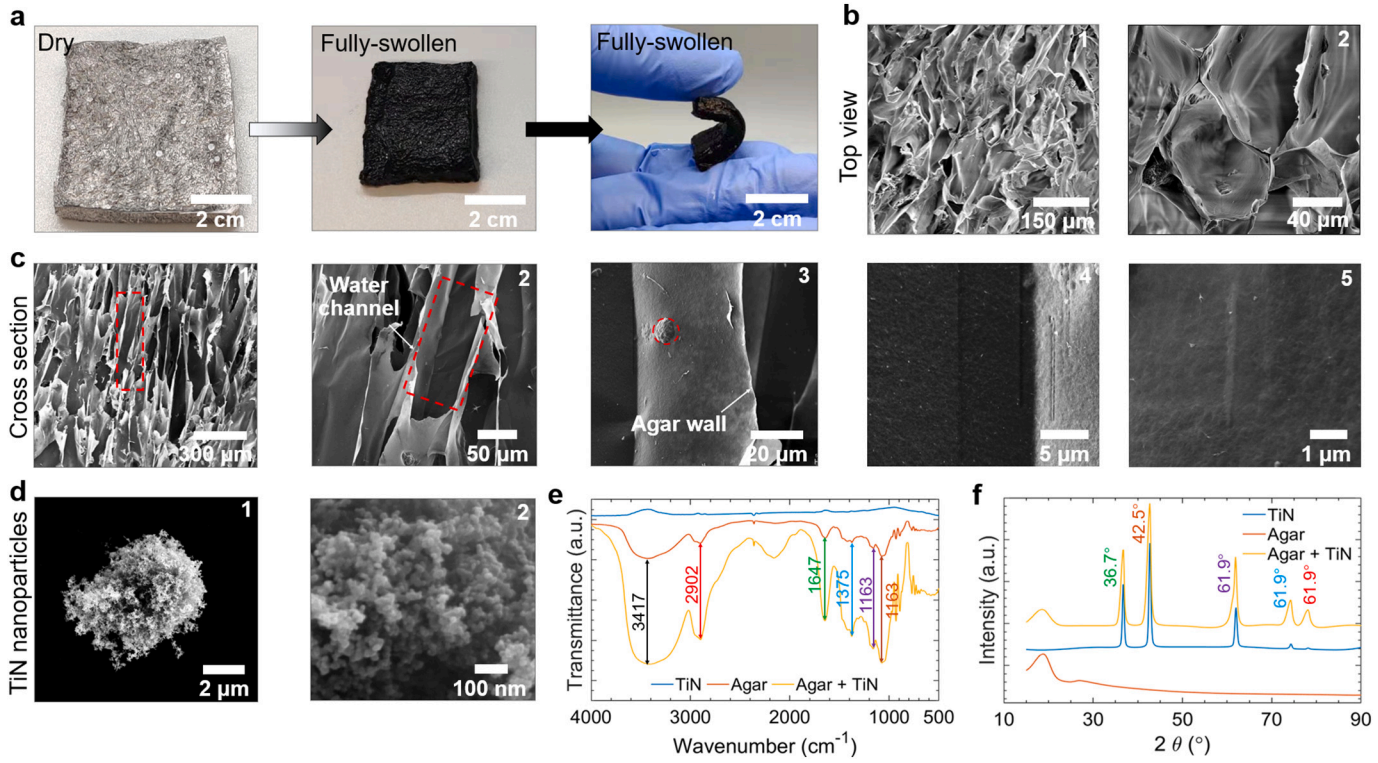

Fig. 2. Self-assembly fabrication and characterizations of ATHEs. (a) Photographs of ATHE 2 in the dry and fully-swollen states. (b) Top-view SEM images showing the porous structure of ATHEs and agar walls. (c) Cross-section of ATHEs elucidating vertically channels for water transportation and rough surface with TiN nanoparticles embedded within the agar walls. Square dash circles are water channels. (d) SEM images illustrating the surface topographies of TiN nanoparticles. (e) FTIR and (f) XRD spectra of the pure agar, TiN, and ATHE 2.

excellent solar absorptance (≈ 0.98) in their fully-swollen state over the broad range of solar wavelengths (0.3 μm − 2.5 μm) characterized by the UV–vis-near-infrared (UV–vis-NIR) spectrophotometer (Fig. 3a). This allows for the solar harvesting and conversion of sunlight into thermal energy. Zero transmittance is measured because samples are thick enough to block incident light, and therefore, solar absorptance is equal to unity minus reflectance (Fig. S3†). The solar absorptance of ATHEs is significantly enhanced after the introduction of TiN nanoparticles as photothermal materials. Moreover, the high average solar absorptance of the ATHEs is also demonstrated to be angle-independent from 0° to 60°, rendering it insensitive to variations of sunlight incident angles due to season and time changes (Fig. 3b).

Another major advantage of employing hydrogel as an evaporator is its excellent water absorption capability. Good water absorption can ensure the water supply to the top evaporation region for continuous solar desalination, meanwhile, water that is transported to the top evaporation region can help dissolve the accumulated salt to avoid the salt blockage. A dynamic water contact angle measurement shows that ATHE 2 has a zero contact angle (Fig. 3c), and the high-speed camera exhibits that the water droplet is absorbed by ATHE2 within 1.2 ms (Fig. 3d). ATHE1 and ATHE 3 display similar water absorption behavior to ATHE 2 (Fig. S4†). Furthermore, the tunable water saturation content and transportation rate of the ATHEs is another advantage for solar desalination implementations. Saturation water content is the ratio of the mass of full swollen ATHEs over its original one. Half swollen time means half of the time during which ATHEs become fully swollen. The saturation water content of ATHEs decreases with the increasing of Agar concentrations, illustrating that the swelling behavior of ATHEs can be easily tuned by changing the initial agar/water ratio (Fig. 3e). Meanwhile, the fully-swollen time for ATHEs increases as the agar/water ratio goes up. The water transport rate (saturation water content over fully-swollen time) can be adjusted from 4.93 g min^{-1} to 0.57 g min^{-1} through changing the initial agar/water ratio (Fig. S5†).

Beyond adjustable water transportation, ATHEs can be optimized to exhibit an enhanced heat localization. The low thermal conductivity of ATHEs is imperative to reduce the heat dissipation to the bottom bulk water, thereby enabling heat confinement to the evaporation region. The thermal conductivity of ATHEs both at dry and fully-swollen states are characterized by the transient plane source method (Fig. 3f). These fully-swollen ATHEs exhibit higher thermal conductivity than that of their dry state resulting from the increased water content. The thermal conductivity of ATHEs ranges from 0.47 W m^{-1} K^{-1} to 0.28 W m^{-1} K^{-1} at the fully-swollen state. Considering both the channel size and water content at the fully-swollen state, ATHE 2 is chosen for the solar desalination evaporation experiment since its minimal thermal conductivity can provide the best heat localization effect for enhancing the evaporation rate. To further hinder heat loss from the evaporator to the bottom bulk water, a 10 mm thick PS foam is introduced to act as a thermal insulator between the bulk water and ATHEs (Fig. S6†). Moreover, to further suppress heat loss, instead of placing ATHEs directly in the bulk water, cotton wipes with excellent water supply capabilities are employed as pathways to pump sufficient water to ATHEs for evaporating. The thermal conductivity of wet cotton wipes is 0.65 W m^{-1} K^{-1} that is low enough to prevent significant heat diffusion via the water pathway (Fig. S6†). The cotton wipe consists of hydrophilic cellulose with a strong capillary-wicking ability that can pump sufficient water to ATHEs (Fig. S1†). To validate the effectiveness of advanced heat localization of the PS foam thermal insulator and the cotton wipe water pathway, a thermal camera is used to evaluate the temperature distribution of the evaporation surface for ATHE 2 (Fig. 3g). For pure water without the evaporator, its surface temperature slowly goes up to 35.2 °C but does not stabilize within 50 min. Due to the heat localization effects of the PS foam and cotton wipe, even the pure agar hydrogel evaporator without TiN nanoparticles to absorb solar energy stabilizes at 40 °C within 45 min. The equilibrium temperature of the ATHE 2 evaporation surface direct contact with water stays at 45.6 °C due to the

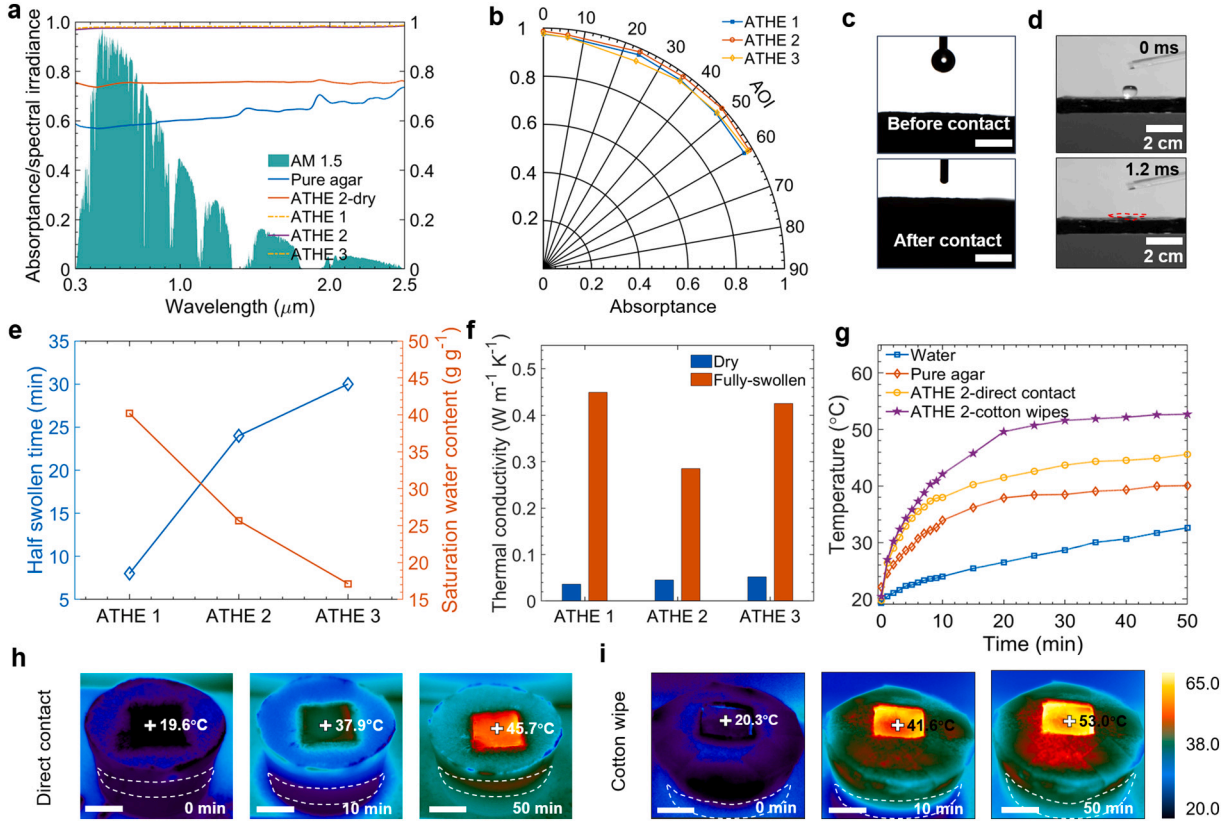

Fig. 3. Tunable water absorption and heat management of ATHEs. (a) Solar absorptance of the pure agar and ATHEs exhibiting against the AM 1.5 spectral irradiance (ASTM G 173). (b) The angle-dependent average solar absorptance of ATHEs. (c) Dynamic water contact angle measurement of ATHE 2. The scale bar is 3 mm. (d) Rapid water absorption behavior of ATHE 2, recorded by a high-speed camera with a rate of 2997 FPS. (e) Swollen behavior and saturation water content of ATHEs. (f) Thermal conductivity of ATHEs at dry and fully-swollen states. (g) Temperature evolutions of the bulk water, the pure agar on a cotton wipe, ATHE 2 directly contact with water, and ATHE 2 on top of a water-supplied cotton wipe. (h) and (i) Thermal images elucidating the temperature distribution of the ATHE 2 for an illumination time of 0, 10, 30, and 60 min (white cross indicates the center of ATHE 2). (h): ATHE 2 directly contact with the bulk water; (i): ATHE 2 placed on top of a cotton wipe with a PS foam as a thermal insulator. The scale bar is 2 cm.

photothermal effect of the TiN nanoparticles and the heat localization effect from its porous structure. While a steady temperature of 53.0 °C is finalized after 48 min when the ATHE 2 is placed on top of the cotton wipe and PS foam. Fig. 3h and i illustrate the temperature distributions of both the evaporation surface and the bulk water. Both the rate of temperature increase and the equilibrium temperature of ATHE 2 with the cotton wipe as the water pathway are higher than that of ATHE 2 direct contact with water. The top small region (white dashed circle) of the bulk water increases to around 41 °C when ATHE 2 is directly immersed into water, while the same region is around 29 °C for the case with the cotton wipe as the water pathway. Therefore, we can conclude that the PS foam, cotton wipe, and PE foam successfully localize heat within the ATHEs for efficient evaporation.

3.3. Solar desalination performance of ATHEs

To demonstrate the enhanced evaporation rate of this advanced heat localization design, we compare the evaporation rate with two different water supply methods under one sun, as shown in Fig. 4a. The experimental setup for evaluating the mass change of ATHEs under one sun illumination is schematically illustrated in Fig. S7†. The evaporation device is placed in the center of the solar irradiance beam of the solar simulator to provide it with collimated sunlight. To quantitatively evaluate the solar evaporation performance of the ATHEs as a 2D evaporator, the sidewalls of ATHEs are tightly surrounded by PE foam with the same thickness of ATHEs and this ensures that only the top surface is the water evaporation and light absorption surface. ATHEs are placed on a PS foam, which is crossed by a cotton wipe strip with super hydrophilicity in the center, to reduce the downward conduction heat loss from the hydrogel to the bulk water beneath. The porous structures and intrinsic hydrophilicity of the cotton wipe render it a superior path of the evaporation device to efficiently transport water to the evaporator. Due to the microchannels of ATHEs and the strong hydrophilicity of agar, ATHEs can continuously pump sufficient water from the cotton wipe for efficient water evaporation. Evaporation rates of ATHE 2 with a cotton wipe as the water pathway and in direct contact with water are 5.15 kg m^{-2} h^{-1} and 2.74 kg m^{-2} h^{-1}, respectively. The evaporation rate using the indirect water supply method is about 2 times that of the direct water supply method. This demonstrates the heat localization effects of using a cotton wipe as the water pathway and a PS foam as the thermal insulator. The localized heat effectively boosts the quick water evaporation with the top region of ATHEs. The evaporation rates of the ATHE 1, 2, and 3 are 3.62, 5.15, and 3.69 kg m^{-2} h^{-1}, respectively, which are 1.4, 2.0, and 1.4 times higher than that of the pure agar with a cotton wipe as the water supply method (Fig. 4b). It is substantiated that the addition of TiN nanoparticles as a photothermal material significantly enhances the evaporation rates of ATHEs. The water evaporation performance under weak sunlight is another key aspect to validate the working performance of ATHEs since the solar intensity varies according to different times of the day and seasons. To investigate the working performance under various solar intensities, we track the evaporation rates of ATHE 2 under varying solar irradiance intensities, as shown in Fig. 4c. Under weak sunlight, ATHE 2 still yields evaporation rates of 2.40 kg m^{-2} h^{-1} and 3.16 kg m^{-2} h^{-1} under 0.5 kW m^{-2} and 0.8 kW m^{-2}, respectively, outperforming most hydrogel evaporators under 1 kW m^{-2}. The evaporation rate of ATHEs under 1.2 sun approaches 6.0

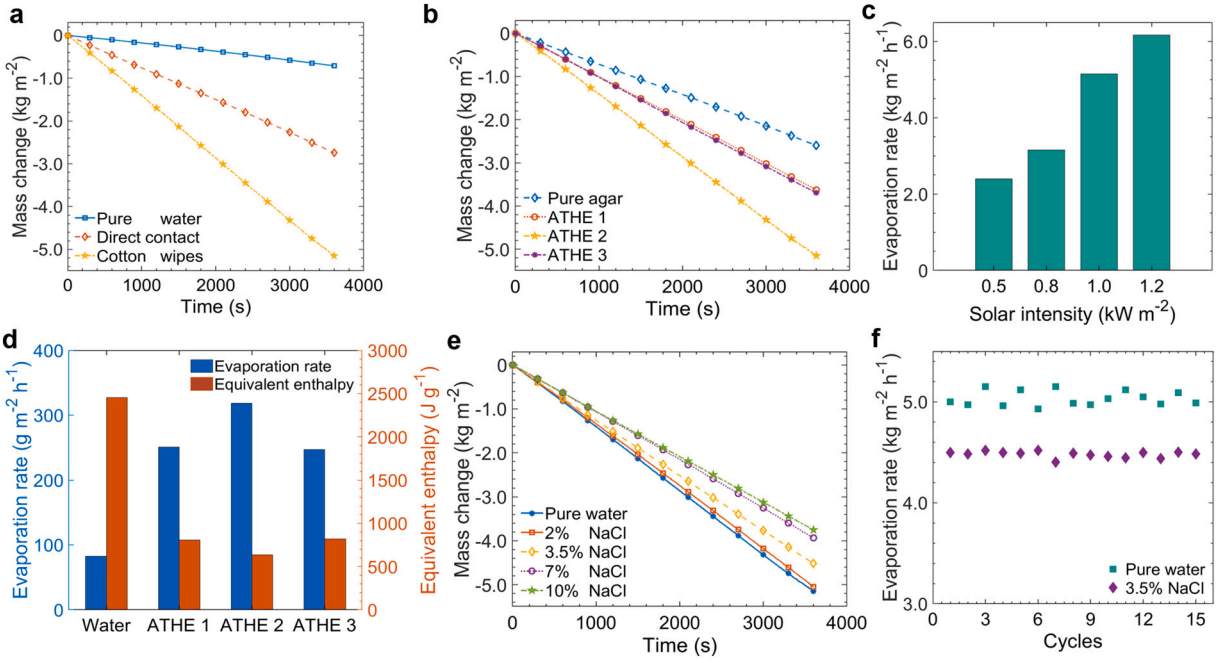

Fig. 4. Solar desalination evaluations of the ATHEs. (a) Mass change of the pure water, ATHE 2 in direct contact with water, and ATHE 2 with a cotton wipe as the water supply path under one sun. (b) Mass change of the pure water, pure agar, and ATHEs under one sun. (c) Evaporation rates of ATHE 2 under varying solar intensities. (d) The evaporation rate of water in a dark environment and calculated equivalent enthalpy of ATHEs. (e) Mass change of ATHE 2 using pure water and NaCl solutions with various salinities. (f) Stability tests of ATHE 2 for continuous 15 h (1 cycle is 1 h).

kg m^{-2} h^{-1}, which validates the excellent evaporation performance owing to higher evaporation surface temperatures. The evaporation efficiency (η) of ATHEs are defined by: $\eta = m \cdot \Delta H_{equ}/C \cdot I$, where m represents the evaporation rate, ΔH_{equ} defines the equivalent enthalpy of water evaporation for ATHEs. C is denoted as the optical concentration of the solar intensity. I is the standard solar irradiance of one sun. Since the evaporation rate of ATHEs is higher than the theoretical values (1.6 kg m^{-2} h^{-1}), the evaporation efficiency of ATHEs will be higher than 1 if we use the corresponding water evaporation enthalpy at 53.0 °C. The equivalent enthalpy of evaporation, ΔH_{equ}, can be evaluated by comparing the evaporation rate under a dark environment of ATHEs and pure water. $\Delta H_{equ} \cdot m_a = \Delta H_0 \cdot m_0$, where ΔH_0 and m_0 refer to the enthalpy of evaporation and evaporation rate of water under the dark environment without ATHEs, respectively. m_a indicates the evaporation rate of ATHEs in the same dark environment. An evaporation efficiency of about 91% can be demonstrated for ATHE 2 due to the excellent heat management for the design of the evaporation device, highly efficient photothermal effects of TiN nanoparticles, and effective water activation to increase the proportion of intermediate water in the hydrogel polymeric network (Fig. S8†) [49], all of which remarkably decreases the enthalpy of water evaporation in ATHEs. This is because of the water interaction between water and plenty of −OH and $-NH_2$ bonds in agar.

Differential scanning calorimetry (DSC) is employed to prove the reduction of enthalpy of water evaporation in polymeric networks of ATHEs. A sharp heat flux signal followed by a sudden decrease after the climax is observed around 90 °C for the pure water (Fig. S9†). However, ATHE 2 shows broad heat flux signal peaks, indicating that the portion of the intermediate water molecules in ATHEs is increased by the strong hydrogen bonds between −OH groups and water molecules (Fig. S9†) [23]. The evaporation rates of ATHEs and pure water in the dark environment further confirm the reduced enthalpy of water evaporation in ATHEs (Fig. S10†). ATHE 2 shows the lowest enthalpy of evaporation of ATHEs (Fig. 4d and Table S1).

Evaporation rates for ATHE 2 in the water of various salinity are illustrated in Fig. 4e. The evaporation rate of ATHE 2 drops with the increase of water salinity. It shows evaporation rates of 4.51 kg m^{-2} h^{-1} and 3.75 kg m^{-2} h^{-1} for water with a salinity of 3.5 wt% and 10 wt%, respectively. This shows the potential of employing ATHEs for desalination in high-salinity brines. The working stability of ATHEs is another essential factor for scalable applications. In a continuous 15 h test of ATHEs, the evaporation rate of ATHE 2 in pure water and 3.5 wt% saltwater under one sun remain nearly constant around 5.1 kg m^{-2} h^{-1} and 4.5 kg m^{-2} h^{-1}, respectively (Fig. 4f). No salt accumulation is observed on the evaporation surface of ATHE 2 during the 15 h continuous sunlight exposure. This demonstrates the stability of the working performance of the ATHEs under solar irradiance.

3.4. *Salt rejection, recyclability, large-scale fabrication, and thermomechanical stability test of ATHEs*

Salt rejection, water quality after desalination, recyclability after lifespan, and scalable fabrication are other critical factors for engineering applications. ATHEs show antifouling functionality when their evaporation surfaces are covered by salt crystals (NaCl) (Fig. 5a). Most of the salt is dissolved and dissipated to the underlying bulk water through the cotton wipe within 4 h, indicating that ATHEs can be self-regenerating during the night to get rid of any daytime-accumulated salt. Although the salt-rejection capabilities of ATHEs are reduced due to the isolated evaporator design that limits the water supply to ATHEs, no salt accumulation happens during the 15 h continuous desalination test (Fig. S11†). To demonstrate the water quality after desalination, seawater is used to track the quality of produced water. After desalination, the salinity of the purified water is two orders of magnitude lower than both standards of the World Health Organization (1) and the US Environmental Protection Agency (0.5) (Fig. 5b). Fig. S12† illustrates the ohmic value of seawater before and after desalination measured by a source measure unit (SMU). The resistance of the purified seawater increases from 12.26 MΩ to 2.0 MΩ after desalination, indicating the excellent seawater purification ability of ATHEs.

While the recyclability of the evaporator is critical to environmental sustainability and cost-effectiveness, it is rarely reported in previous work. ATHEs can be recycled by re-melting to hydrogel solution and

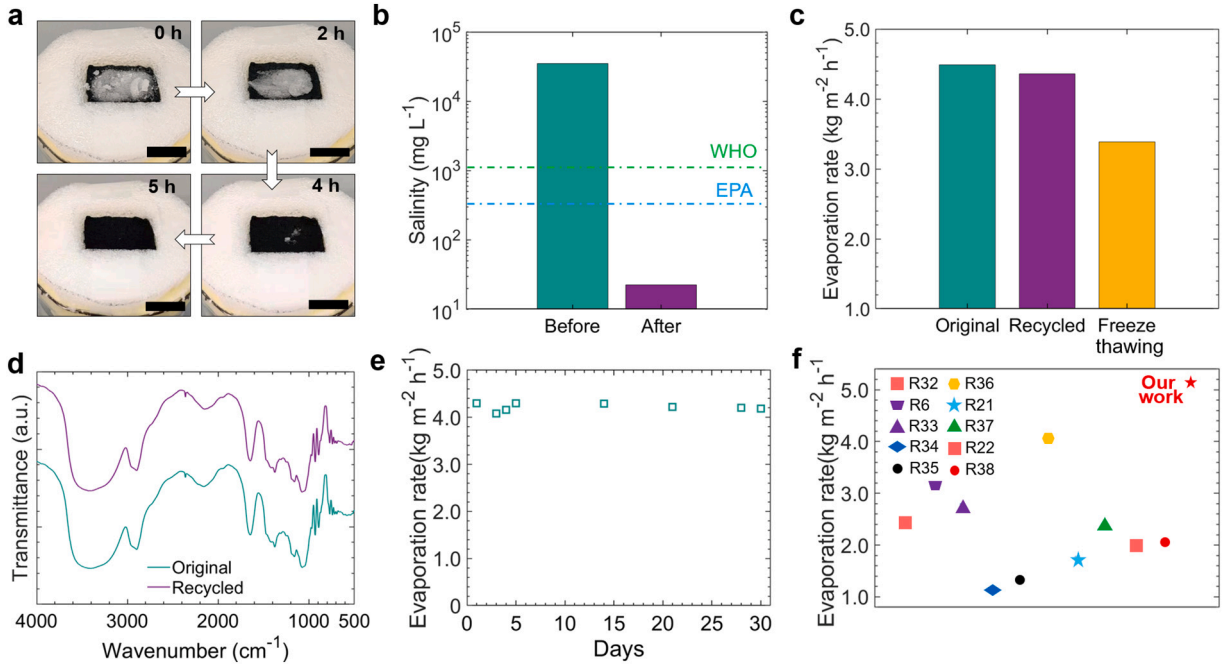

Fig. 5. Salt rejection, recyclability, and scalable fabrication of ATHEs. (a) Salt rejection experiment for ATHE 2 with an initial presence of 1 g salt under one sun. The scale bar is 2 cm. (b) Salinity of the seawater before and after desalination. (c) Evaporation rates of the original ATHE 2, the recycled ATHE 2, and ATHE fabricated by the repeated freeze-thaw process. (d) FTIR spectra of the original and recycled ATHE 2. (e) Long-term evaporation rates of ATHE 2 immersed into 3.5 wt % NaCl solutions for 30 days. (f) Water evaporation rate comparison between ATHE 2 and other previously reported devices. Details are listed in Table S2 [6,31,32,42–48].

following the same unidirectional frozen and freeze-drying process. The evaporation performance of the recycled ATHE 2 is 97% of the original one (4.36/4.49 ≈ 97%) (Fig. 5c). The FTIR transmittance spectra of the ATHE 2 and recycled ATHE 2 also illustrate their consistency in the presence of chemical components (Fig. 5d). ATHEs can also be scalably fabricated by a repeated freeze-thawing process with some scarification of the evaporation rate (Fig. 5c). The evaporation rate of ATHE 2 remains stable around 4.4 kg m^{-2} h^{-1} after being immersed in the 3.5 wt% NaCl solution for 30 days and subsequently take it out to test the evaporation rate after certain days (Fig. 5e), indicating that ATHEs are stable for potential long-term solar desalination applications. Fig. 5f and Table S2, show a detailed comparison of the evaporation rate of ATHEs with other previously reported devices. The evaporation rate of ATHEs tops this collection of data. With the advantages of high evaporation rate, cost-effectiveness, and scalable fabrication methods, ATHEs can easily be integrated into large-scale applications considering the abundant raw material resources. The cost of ATHE 2 is around 5.04 USD m^{-2} (Table S3), while, for scalable engineering applications, the relatively expensive TiN nanoparticles can be replaced by other alternatives, such as carbon nanoparticles derived from carbonized manure [24,25] and wood [50], to reduce the raw photothermal materials cost. Chitosan [51,52], glean gum [53], and agarose [54] can be developed as alternatives for the agar to enrich the raw materials and they are all environmentally friendly and abundant in nature.

The interaction between TiN nanoparticles and the agar hydrogel network plays a key role in the stability of ATHEs for real-life engineering applications. To evaluate this, we conduct a series of dynamic experiments, including the ultrasonic test, rotation test, and heating test, to study the thermomechanical stability of ATHEs.

Fig. S13 shows the stability test of ATHEs in ultrasonic water. This process can evaluate the adhesion stability between agar and TiN nanoparticles. ATHE 2 with a dimension of 25 mm × 25 mm floating on water in a 250 ml glass beaker. The glass beaker is placed in the water tank of an ultrasonic machine (90 W, 47 kHz). The ultrasonic process lasted for 60 min and no TiN nanoparticles is falling off during this process, as illustrated in photographs of Fig. S13b-d.

For the adhesion stability test in swirling water (Fig. S14), ATHE 2 with a size of 30 mm × 30 mm × 5 mm is floating on the water within a glass beaker. The water is stirred by a magnetic stirring bar with a constant rotation speed of 550 r min^{-1}. Meanwhile, a whirlpool is formed due to the high-speed rotation of the magnetic bar. ATHEs rotate with water flow and stay stable. After the test, no visual changes and no nanoparticles are falling off from the evaporator.

To further validate the thermal stability of ATHEs, they are placed in 65 °C warming water for 1 h. No nanoparticles fall off from ATHEs, demonstrating their excellent thermal stability. For large-scale engineering applications, the superior thermomechanical stability of ATHEs will help their implementations.

4. Conclusions

In summary, ATHEs are demonstrated to achieve a rapid evaporation rate of 5.15 kg m^{-2} h^{-1} in a 2D structure with an evaporation efficiency of 91% under one sun irradiance and boast a high-quality freshwater yield. Highly efficient solar evaporation results from tunable water transportation within vertically aligned channels. The water absorption, enhanced by strong capillary force in unidirectional water pathways in ATHEs, provides quick water absorption from the bulk water reservoir to the evaporation surface. The saturation water content in polymeric networks can be tuned by changing the concentrations of raw hydrogel solutions. A solar absorptance of 0.98 is induced by the inclusion of TiN nanoparticles as photothermal materials and these nanoparticles are embedded within the polymeric agar walls. After absorbing solar energy, these nanoparticles transfer heat to the surrounding agar and water for evaporation. Quick capillary water pumping in the vertical channels together with ion diffusion leads to effective salt drainage from the vaporized saltwater to protect salt from accumulating, thus ensuring continuous and rapid solar desalination. The porous structure of ATHEs contributes greatly to their low thermal conductivity, thereby enabling thermal energy confinement within the water/air interfacial region to

power water evaporation with significantly reduced enthalpy of vaporization. Moreover, a strategy for the fabrication of an ocean biomass-derived hydrogel evaporator with vertically aligned and controllable tunnels has been developed by an integrated ice template-induced self-assembly and freeze-drying process. The indirect water supply method and heat localization strategy of employing the cotton as the water transportation and salt drainage pathway, using PS foam as the thermal barrier between ATHEs and the bulking water, and utilizing PE foam as the thermal insulator between the ATHEs and surrounding air successfully reduce the heat loss to the bulk water and surrounding air and localize heat within the top small evaporation region of ATHEs. Taking advantage of these strategies discussed above, a water evaporation rate of 5.15 kg m^{-2} h^{-1} and a solar desalination rate of 4.0 kg m^{-2} h^{-1} under the irradiance of one sun (1 kW m^{-2}) were achieved by this photothermal evaporator. Moreover, we validate that repeated freeze-thaw process with the removal of the time- and cost-ineffective freeze-drying process still yields a desalination rate of 3.39 kg m^{-2} h^{-1}. The photothermal material, TiN nanoparticles, can also be replaced with inexpensive materials such as carbon nanoparticles derived from carbonized biowaste (manure, wood, or sawdust). The recyclability of the ATHEs is also attained without sacrificing the high desalination rate. Large-scale fabrication demonstrations, high recyclability potential, and the abundantly available raw material of agar feature ATHEs an ideal candidate for industrial solar evaporation and desalination applications.

CRediT authorship contribution statement

Yanpei Tian: Conceptualization, Methodology, Investigation, Writing - original draft preparation. **Xiaojie Liu:** Methodology, Formal analysis, Investigation. **Shilin Xu:** Methodology, Formal analysis, Investigation. **Andrew Caratenuto:** Validation, Characterization. **Ying Mu:** Characterization. **Ziqi Wang:** Validation, Characterization. **Fangqi Chen:** Characterization. Ruizhe Yang: Methodology. **Jun Liu:** Methodology, Writing – review & editing. **Marilyn** L. **Minus:** Methodology, Writing – review & editing. **Yi Zheng:** Conceptualization, Supervision, Project administration, Writing – review & editing, Funding acquisition.

Declaration of competing interest

The authors declare no conflict of interest.

Acknowledgments

This project is supported by the National Science Foundation through grant number CBET-1941743.

Appendix A. Supplementary data

Supplementary data to this article can be found online at https://doi.org/10.1016/j.desal.2021.115449.

References

[1] M.M. Mekonnen, A.Y. Hoekstra, Four billion people facing severe water scarcity, Sci. Adv. 2 (2) (2016), e1500323.
[2] L.N.O. Behind, United Nations World Water Development Report 2019, 2019.
[3] P.J. Alvarez, C.K. Chan, M. Elimelech, N.J. Halas, D. Villagrán, Emerging opportunities for nanotechnology to enhance water security, Nat. Nanotechnol. 13 (8) (2018) 634–641.
[4] J.R. Werber, C.O. Osuji, M. Elimelech, Materials for next-generation desalination and water purification membranes, Nat. Rev. Mater. 1 (5) (2016) 1–15.
[5] Y. Guo, X. Zhou, F. Zhao, J. Bae, B. Rosenberger, G. Yu, Synergistic energy nanoconfinement and water activation in hydrogels for efficient solar water desalination, ACS Nano 13 (7) (2019) 7913–7919.
[6] Y. Guo, H. Lu, F. Zhao, X. Zhou, W. Shi, G. Yu, Biomass-derived hybrid hydrogel evaporators for cost-effective solar water purification, Adv. Mater. 32 (11) (2020) 1907061.
[7] Y. Zhang, T. Xiong, D.K. Nandakumar, S.C. Tan, Structure architecting for salt-rejecting solar interfacial desalination to achieve high-performance evaporation with in situ energy generation, Adv. Sci. 7 (9) (2020), 1903478.
[8] J. He, Y. Fan, C. Xiao, F. Liu, H. Sun, Z. Zhu, W. Liang, A. Li, Enhanced solar steam generation of hydrogel composite with aligned channel and shape memory behavior, Compos. Sci. Technol. 204 (2021), 108633.
[9] J. Li, M. Du, G. Lv, L. Zhou, X. Li, L. Bertoluzzi, C. Liu, S. Zhu, J. Zhu, Interfacial solar steam generation enables fast-responsive, energy-efficient, and low-cost off-grid sterilization, Adv. Mater. 30 (49) (2018) 1805159.
[10] L. Zhao L. Wang J. Shi X. Hou Q. Wang Y. Zhang Y. Wang N. Bai J. Yang J. Zhang , et al., Shape-programmable interfacial solar evaporator with salt-precipitation monitoring function, ACS Nano.
[11] K. Xu, C. Wang, Z. Li, S. Wu, J. Wang, Salt mitigation strategies of solar-driven interfacial desalination, Adv. Funct. Mater. 31 (8) (2021) 2007855.
[12] N. Li, L. Qiao, J. He, S. Wang, L. Yu, P. Murto, X. Li, X. Xu, Solar-driven interfacial evaporation and self-powered water wave detection based on an all-cellulose monolithic design, Adv. Funct. Mater. 31 (7) (2021), 2008681.
[13] P. Qiu, F. Liu, C. Xu, H. Chen, F. Jiang, Y. Li, Z. Guo, Porous three-dimensional carbon foams with interconnected microchannels for high-efficiency solar-to-vapor conversion and desalination, J. Mater. Chem. A 7 (21) (2019) 13036–13042.
[14] P. Zhang, J. Li, L. Lv, Y. Zhao, L. Qu, Vertically aligned graphene sheets membrane for highly efficient solar thermal generation of clean water, ACS Nano 11 (5) (2017) 5087–5093.
[15] X. Cao, T. Wang, L. Jiao, Transition-metal (fe, co, and ni)-based nanofiber electrocatalysts for water splitting, Adv. Fiber Mater. (2021) 1–19.
[16] Z. Liu, Z. Zhou, N. Wu, R. Zhang, B. Zhu, H. Jin, Y. Zhang, M. Zhu, Z. Chen, Hierarchical photothermal fabrics with low evaporation enthalpy as heliotropic evaporators for efficient, continuous, salt-free desalination, ACS Nano 15 (8) (2021) 13007–13018.
[17] Z. Liu, Q. Zhong, N. Wu, H. Zhou, L. Wang, L. Zhu, N. Jiang, B. Zhu, Z. Chen, M. Zhu, Vertically symmetrical evaporator based on photothermal fabrics for efficient continuous desalination through inversion strategy, Desalination 509 (2021), 115072.
[18] Y. Wang, C. Wang, X. Song, S.K. Megarajan, H. Jiang, A facile nanocomposite strategy to fabricate a rgo–mwcnt photothermal layer for efficient water evaporation, J. Mater. Chem. A 6 (3) (2018) 963–971.
[19] J. Zhao, Y. Yang, C. Yang, Y. Tian, Y. Han, J. Liu, X. Yin, W. Que, A hydrophobic surface enabled salt-blocking 2d ti 3 c 2 mxene membrane for efficient and stable solar desalination, J. Mater. Chem. A 6 (33) (2018) 16196–16204.
[20] P. Zhang, Q. Liao, T. Zhang, H. Cheng, Y. Huang, C. Yang, C. Li, L. Jiang, L. Qu, High throughput of clean water excluding ions, organic media, and bacteria from defect-abundant graphene aerogel under sunlight, Nano Energy 46 (2018) 415–422.
[21] X. Meng, W. Xu, Z. Li, J. Yang, J. Zhao, X. Zou, Y. Sun, Y. Dai, Coupling of hierarchical al 2 o 3/tio 2 nanofibers into 3d photothermal aerogels toward simultaneous water evaporation and purification, Adv. Fiber Mater. 2 (2) (2020) 93–104.
[22] J. Zeng, Q. Wang, Y. Shi, P. Liu, R. Chen, Osmotic pumping and salt rejection by polyelectrolyte hydrogel for continuous solar desalination, Adv. Energy Mater. 9 (38) (2019), 1900552.
[23] F. Zhao, X. Zhou, Y. Shi, X. Qian, M. Alexander, X. Zhao, S. Mendez, R. Yang, L. Qu, G. Yu, Highly efficient solar vapour generation via hierarchically nanostructured gels, Nat. Nanotechnol. 13 (6) (2018) 489–495.
[24] Y. Tian, X. Liu, Z. Wang, A. Caratenuto, F. Chen, Y. Wan, Y. Zheng, Carbonized cattle manure-based photothermal evaporator with hierarchically bimodal pores for solar desalination in high-salinity brines, Desalination 520 (2021), 115345.
[25] Y. Tian, X. Liu, J. Li, Y. Deng, J.A. DeGiorgis, S. Zhou, A. Caratenuto, M.L. Minus, Y. Wan, G. Xiao, et al., Farm-waste-derived recyclable photothermal evaporator, Cell Rep. Phys. Sci. 2 (9) (2021), 100549.
[26] H.N. Panchal, Performance analysis of solar still with cow dung cakes and blue metal stones, Front. Energy 9 (2) (2015) 180–186.
[27] H. Panchal, J. Patel, S. Chaudhary, A comprehensive review of solar cooker with sensible and latent heat storage materials, Int. J. Ambient Energy 40 (3) (2019) 329–334.
[28] M. Vaka, R. Walvekar, M. Khalid, P. Jagadish, N.M. Mubarak, H. Panchal, Synthesis of hybrid graphene/tio2 nanoparticles based high-temperature quinary salt mixture for energy storage application, J. Energy Storage 31 (2020), 101540.
[29] M. Patel, C. Patel, H. Panchal, Performance analysis of conventional triple basin solar still with evacuated heat pipes, corrugated sheets and storage materials, Groundw. Sustain. Dev. 11 (2020), 100387.
[30] T. Xu, Y. Xu, J. Wang, H. Lu, W. Liu, J. Wang, Sustainable self-cleaning evaporator for long-term solar desalination using gradient structure tailored hydrogel, Chem. Eng. J. 128893 (2021).
[31] X. Chen, Z. Wu, D. Lai, M. Zheng, L. Xu, J. Huo, Z. Chen, B. Yuan, M.-L. Fu, Resilient biomass-derived hydrogel with tailored topography for highly efficient and long-term solar evaporation of high-salinity brine, J. Mater. Chem. A 8 (43) (2020) 22645–22656.
[32] Y. Xu, X. Xiao, X. Fan, Y. Yang, C. Song, Y. Fan, Y. Liu, Low cost, facile, environmentally friendly all biomass-based squid ink-starch hydrogel for efficient solar-steam generation, J. Mater. Chem. A 8 (45) (2020) 24108–24116.
[33] G.O. Phillips, P.A. Williams, Handbook of Hydrocolloids, Elsevier, 2009.
[34] O. Duman, T.G. Polat, C.Ö. Diker, S. Tunç, Agar/-carrageenan composite hydrogel adsorbent for the removal of methylene blue from water, Int. J. Biol. Macromol. 160 (2020) 823–835.
[35] A.K. Sonker, M. Belay, K. Rathore, K. Jahan, S. Verma, G. Ramanathan, V. Verma, Crosslinking of agar by diisocyanates, Carbohydr. Polym. 202 (2018) 454–460.
[36] L. Taiz, E. Zeiger, I.M. Møller, A. Murphy, Plant Physiology and Development, 6, Sinauer Associates Incorporated, 2015.

[37] Y. Li, C. Lin, Z. Wu, Z. Chen, C. Chi, F. Cao, D. Mei, H. Yan, C.Y. Tso, C.Y. Chao, et al., Solution-processed all-ceramic plasmonic metamaterials for efficient solar–thermal conversion over 100–727Â° c, Adv. Mater. 33 (1) (2021) 2005074.
[38] M. Tako, M. Higa, K. Medoruma, Y. Nakasone, A highly methylated agar from red seaweed, gracilaria arcuata, Bot. Mar. 42 (6) (1999) 513–517.
[39] S. Kumar, J.C. Boro, D. Ray, A. Mukherjee, J. Dutta, Bionanocomposite films of agar incorporated with zno nanoparticles as an active packaging material for shelf life extension of green grape, Heliyon 5 (6) (2019), e01867.
[40] V. Hasija, K. Sharma, V. Kumar, S. Sharma, V. Sharma, Green synthesis of agar/gum arabic based superabsorbent as an alternative for irrigation in agriculture, Vacuum 157 (2018) 458–464.
[41] H. Zhang, F. Li, Q. Jia, Preparation of titanium nitride ultrafine powders by sol–gel and microwave carbothermal reduction nitridation methods, Ceram. Int. 35 (3) (2009) 1071–1075.
[42] X. Zhou, F. Zhao, Y. Guo, Y. Zhang, G. Yu, A hydrogel-based antifouling solar evaporator for highly efficient water desalination, Energy Environ. Sci. 11 (8) (2018) 1985–1992.
[43] F. Zhu, L. Wang, B. Demir, M. An, Z.L. Wu, J. Yin, R. Xiao, Q. Zheng, J. Qian, Accelerating solar desalination in brine through ion activated hierarchically porous polyion complex hydrogels, Mater. Horiz. 7 (12) (2020) 3187–3195.
[44] S.H. Park, J.H. Park, J. Kim, S.J. Lee, Simultaneous solar-driven seawater desalination and spontaneous power generation using polyvalent crosslinked polypyrrole/alginate hydrogels, Desalination 500 (2021), 114900.
[45] C. Xiao, W. Liang, Q.-M. Hasi, L. Chen, J. He, F. Liu, C. Wang, H. Sun, Z. Zhu, A. Li, Ag/polypyrrole co-modified poly (ionic liquid) s hydrogels as efficient solar generators for desalination, Mater. Today Energy 16 (2020), 100417.
[46] H. Su, J. Zhou, L. Miao, J. Shi, Y. Gu, P. Wang, Y. Tian, X. Mu, A. Wei, L. Huang, et al., A hybrid hydrogel with protonated g-c3n4 and graphene oxide as an efficient absorber for solar steam evaporation, Sustain. Mater. Technol. 20 (2019), e00095.
[47] H. Lu, W. Shi, F. Zhao, W. Zhang, P. Zhang, C. Zhao, G. Yu, High-yield and low-cost solar water purification via hydrogel-based membrane distillation, Adv. Funct. Mater. 2101036 (2021).
[48] Z. Sun, J. Wang, Q. Wu, Z. Wang, Z. Wang, J. Sun, C.-J. Liu, Plasmon based double-layer hydrogel device for a highly efficient solar vapor generation, Adv. Funct. Mater. 29 (29) (2019) 1901312.
[49] X. Zhou, F. Zhao, Y. Guo, B. Rosenberger, G. Yu, Architecting highly hydratable polymer networks to tune the water state for solar water purification, Sci. Adv. 5 (6) (2019), eaaw5484.
[50] G. Xue, K. Liu, Q. Chen, P. Yang, J. Li, T. Ding, J. Duan, B. Qi, J. Zhou, Robust and low-cost flame-treated wood for high-performance solar steam generation, ACS Appl. Mater. Interfaces 9 (17) (2017) 15052–15057.
[51] F. Wang, D. Wei, Y. Li, T. Chen, P. Mu, H. Sun, Z. Zhu, W. Liang, A. Li, Chitosan/reduced graphene oxide-modified spacer fabric as a salt-resistant solar absorber for efficient solar steam generation, J. Mater. Chem. A 7 (31) (2019) 18311–18317.
[52] X. Liu, Y. Tian, Y. Wu, A. Caratenuto, F. Chen, S. Cui, J.A. DeGiorgis, Y. Wan, Y. Zheng, Seawater desalination derived entirely from ocean biomass, J. Mater. Chem. A 9 (39) (2021) 22313–22324.
[53] X. Liu, Y. Tian, Y. Wu, F. Chen, Y. Mu, M.L. Minus, Y. Zheng, Fully biomass-based hybrid hydrogel for efficient solar desalination with salt self-cleaning property, ACS Appl. Mater. Interfaces 13 (36) (2021) 42832–42842.
[54] X. Wu, M.E. Robson, J.L. Phelps, J.S. Tan, B. Shao, G. Owens, H. Xu, A flexible photothermal cotton-cus nanocage-agarose aerogel towards portable solar steam generation, Nano Energy 56 (2019) 708–715.